Fundamental Mechanics and Precision Control of Optical Axis Stability and Parallelism in Multi-Sensor Electro-Optical Pods

Zhihui Huang[1,*], Shengwei Chi[1] and Lei Zhu[2]

[1] School of Mechanical Engineering, Wuxi Institute of Technology, Wuxi, 214000, China

[2] Xi'an Institute of Applied Optics, Xi'an, 710000, China

INFORMATION

Keywords:
Optical axis stability
multi-sensor alignment
thermal-mechanical coupling
error propagation modeling
model-experiment validation

DOI: 10.23967/j.rimni.2025.10.67662

SCIPEDIA Revista Internacional de Métodos Numéricos para Cálculo y Diseño en Ingeniería

Revista Internacional Métodos numéricos para cálculo y diseño en ingeniería RIMNI in cooperation with CIMNE

Fundamental Mechanics and Precision Control of Optical Axis Stability and Parallelism in Multi-Sensor Electro-Optical Pods

Zhihui Huang[1,*], **Shengwei Chi**[1] **and Lei Zhu**[2]

[1]School of Mechanical Engineering, Wuxi Institute of Technology, Wuxi, 214000, China

[2]Xi'an Institute of Applied Optics, Xi'an, 710000, China

ABSTRACT

Modern electro-optical pods incorporate multi-spectral sensors for reconnaissance, target acquisition, and laser designation, where sub-milliradian optical axis stability and inter-sensor parallelism are critical for mission success. This paper establishes a unified theoretical framework combining rigid-body kinematics and deformable body mechanics to develop a physics-based stability metric through screw theory formulation, expressing the optical axis dynamics as $\dot{\mathbf{O}} = [\omega]_\times \mathbf{O} + \mathbf{v}$, with thermo-mechanical constraints $\|[\omega]_\times \mathbf{O}\| < \epsilon_\omega$, $\|\mathbf{v}\| < \epsilon_\mathbf{v}$ for engineering implementation. A novel computational geometry method evaluates multi-sensor alignment errors by solving $\mathbf{E}_i = \mathbf{s}_i - (\mathbf{s}_i \cdot \hat{\mathbf{O}})\hat{\mathbf{O}} + \mathbf{J}_T \Delta T + \mathbf{J}_g \mathbf{g}$, where $\mathbf{J}_T$ and $\mathbf{J}_g$ represent thermal and gravitational Jacobians. The rigid-flexible coupling model with multi-point constraints (MPC) reveals thermal dominance (0.49 mrad IR sensor pitch displacement at 60°C, 272× gravitational effect), material sensitivity (CTE mismatch contributing 68% of TV sensor's azimuthal error), and cross-axis coupling (19% LD error amplification under thermal gradients). However, due to the limitations of current experimental conditions, the experimental validation is mainly carried out in controlled environments. The current experimental validation shows <5% deviation between predicted and measured parallelism errors across −20°C to 60°C. In the future, we will supplement the evaluation of the robustness of the control method through existing simulation verifications (such as adding vibration and temperature disturbance models) in the "experimental discussion" or "prospect" section, and clarify the research plan for actual environment testing. The framework provides design guidelines for optimal sensor placement minimizing $\|\mathbf{J}_T\|_F$, temperature-dependent calibration protocols, and 0.1 mrad allocable margin for manufacturing tolerances. This methodology advances electro-optical system engineering from empirical tuning to model-driven optimization, demonstrating 0.12 mrad (3σ) stability in field tests under ISO 9022 environmental stress profiles, with key innovations including the first integration of Lie algebra kinematics with FEM-based deformation analysis for optical systems and physics-informed error budgeting separating thermal, mechanical, and alignment components.

OPEN ACCESS

Received: 09/05/2025

Accepted: 14/07/2025

Published: 27/10/2025

DOI
10.23967/j.rimni.2025.10.67662

Keywords:
Optical axis stability
multi-sensor alignment
thermal-mechanical coupling
error propagation modeling
model-experiment validation

*Correspondence: Zhihui Huang (huangzh@wxit.edu.cn).

1 Introduction

The parametric fidelity of optical axis stability and multi-sensor parallelism constitutes a critical determinant in the targeting precision of electro-optical pod systems [1–3]. These parameters are also essential in ensuring the accuracy and reliability of multiple agile optical satellites, where precise scheduling and task management are crucial for mission success [4]. In the context of Optical Character Recognition (OCR), the alignment and stability of optical systems play a significant role in improving recognition accuracy, especially when dealing with complex scripts like Arabic, which require high precision in character identification [5]. Additionally, the study of bifurcation techniques in thermo-mechanical coupling analysis, as seen in the work on the Biswas-Arshed model, provides valuable insights into the behavior of optical systems under varying thermal conditions, which is relevant to maintaining optical axis stability [6]. These studies collectively highlight the importance of addressing both the mechanical and thermal aspects of optical systems to ensure their performance and reliability. These specifications serve as paramount performance metrics for laser designation systems and stabilized tracking platforms, conse-quently receiving substantial scholarly and engineering attention within the electro-optical community. Zhou et al. [7] proposed a novel calibration model for fisheye cameras using a stereo pair of images with a colinear constraint of the main optical axis and epipolar line orthogonality-transverse axis, achieving high calibration accuracy verified through an indoor 3-D calibration field. Marsocci et al. [8] introduced X-STARS, a method for cross-sensor self-supervised training and alignment in remote sensing, using a Multi-Sensor Alignment Dense loss (MSAD) to align representations across sensors with different resolutions, and demonstrates its effectiveness on various classification and segmentation tasks. To ensure mission-critical reliability, rigorous compliance with these parameters must be demonstrated prior to system deployment, complemented by precision ground calibration protocols to verify operational conformance [9]. Advanced pod configurations further incorporate in-flight auto-collimation systems to maintain real-time targeting accuracy during precision engagement scenarios. Contemporary technological advancements in optical axis control have crystallized around three principal research domains:

1.1 Precision Optical Alignment Methodologies

Sophisticated techniques encompassing both monocular optical axis optimization and poly-chromatic sensor array parallelism have emerged [10,11]. State-of-the-art implementations leverage adaptive opto-mechanical control architectures and self-correcting optical configurations to achieve micron-level alignment stability under dynamic operational constraints.

1.2 Parallelism Metrology Systems

A hierarchical calibration paradigm has been developed, integrating, Laboratory-grade interfero-metric alignment systems (sub-arcsecond accuracy), Field-deployable portable collimators, Embedded au-to-collimation modules for real-time aerial compensation [12–15]. This multi-tiered approach ensures spectral alignment fidelity across diverse environmental regimes.

1.3 First-Principles Stability Analysis

Fundamental investigations into environmental perturbation effects (thermal gradients, structural harmonics, and quasi-static loads) have yielded predictive modeling frameworks. These incorporate Coupled thermo-elastic simulations, Frequency-domain vibration analysis and Nonlinear stress-optic coupling models. While alignment and metrology technologies have achieved technological maturity during integration and testing phases, theoretical underpinnings of optical axis stability remain

predominantly confined to preliminary design analysis [16–18]. Current literature exhibits significant lacunae, particularly regarding, the paucity of first-principles treatments of multi-sensor parallelism, inadequate mathematical formalization of constraint-based models. Operational constraints further compound these theoretical shortcomings, mechanical compensation during ground calibration exhibits diminishing returns beyond 200 μm shim thickness due to induced structural compliance, aerial electronic compensation faces human-machine interface limitations ($\leq$15% image plane offset) to prevent target reacquisition latency. Systems engineering principles dictate that 72 $\pm$ 5% of final performance is irrevocably determined during conceptual design phases. Consequently, this work establishes, i) A Lie-algebraic formulation of multi-sensor kinematic chains. ii) Thermomechanical error propagation models. iii) Field-validated calibration transfer functions. The resultant framework advances electro-optical system design from empirical iteration to model-driven optimization, demonstrating 0.12 mrad (3σ) stability in operational environments per MIL-STD-810H protocols.

1.4 Main Contribution of This Paper

This paper makes fundamental advancements in the theoretical understanding and practical implementation of optical axis stability and parallelism in multi-sensor electro-optical pods through three key contributions,

1. Unified Kinematic-Dynamic Stability Criterion We establish a first-principles stability metric derived from screw theory and Lie algebra, formalizing optical axis dynamics as $\dot{\mathbf{O}} = [\omega]_\times \mathbf{O} + \mathbf{v}$ with thermo-mechanical constraints $\left\|[\omega]_\times \mathbf{O}\right\| < \epsilon_\omega$, $\|v\| < \epsilon v$. This framework bridges the gap between rigid-body kinematics and deformable structural analysis, ena-predictive stability assessment under operational loads.

2.Physics-Informed Parallelism Error Propagation Model A novel computational geometry method decomposes multi-sensor alignment errors into thermal, mechanical, and intrinsic components via: $\mathbf{E}_i = \mathbf{s}_i - (\mathbf{s}_i \cdot \hat{\mathbf{O}})\hat{\mathbf{O}} + \mathbf{J}_T \Delta T + \mathbf{J}_g \mathbf{g}$. Where the derived thermal Jacobian $\mathbf{J}_T$ quantifies CTE mismatch effects (accounting for 68% of TV sensor azimuthal error), while the gravitational Jacobian $\mathbf{J}_g$ confirms negligible drift (<0.1 mrad/g).

3. Validated Rigid-Flexible Coupling Optimization The proposed MPC-based simulation mode l demonstrates 0.12 mrad (3σ) stability in field tests under ISO 9022 profiles, achieving, 1) Optimal sensor placement minimizing $\|\mathbf{J}_T\|_F$. 2) Temperature-dependent error compensation matrices reducing thermal drift by 83%. 3) 0.1 mrad tolerance budget for manufacturing variances. These contributions collectively transition electro-optical system design from empirical tri-al-and-error to model-driven optimization, as evidenced by, 5× improvement in aerial auto-collimation accuracy (0.49 $\rightarrow$ 0.098 mrad at 60°C), 40% reduction in ground calibration iterations. Compliance with MIL-STD-810H environmental stress requirements. This paper provides both theoretical foundations for multi-sensor parallelism analysis and actionable tools for precision optomechanical system engineering.

2 Rigid-Flexible Coupling Modeling and Stability-Parallelism Co-Optimization

The electro-optical pod's performance hinges on two interdependent factors: the stability of individual sensor optical axes and the parallelism across multi-sensor assemblies. To address this, we propose a rigid-flexible coupling simulation framework that unifies rigid-body kinematics for stability analysis and multi-point constraints (MPC) for parallelism error prediction. Our method begins by de-riving a physics-based stability criterion from screw theory, where optical axis motion is decomposed into exponential rotation $e^{[\omega]\times t}\mathbf{O}_0$ and and linear translation vt, with stability enforced via dynamic equilibrium $[\omega]_\times \mathbf{O}_0 + v = 0$. Next, we introduce a sensor-aware parallelism metric,

projecting each sensor's axis S_i onto the reference optical axis $0(t)$ to isolate misalignment erro $\mathbf{E}_i$, while incorporating thermal/mechanical displacements through MPC-based coupling. Simulations reveal that thermal gradients dominate optical axis drift (e.g., 0.49 mrad pitch displacement at 60°C), far exceeding gravitational effects. By integrating these components into a single optimization loop—linking kinematic stability, geometric parallelism, and environmental disturbances—our approach bridges theoretical modeling with actionable design insights, enabling precision enhancement in electro-optical pods under real-world operational stresses. The enhanced optical axis stability analysis with integrate formulations is given in Algorithm 1.

Algorithm 1: Enhanced optical axis stability analysis with integrated for-mulations (Author-Derived Summary)

procedure INPUT: $O_0, \omega, v, \{S_i\}_{i=1}^{n}, \{D_j\}_{j=1}^{k}$
  Initialize:
    Initial optical axis vector $\mathbf{O}_0$, angular/translayional velocities ω, v
    Sensor vectors $\{s_i\}$, displacement matrices $\{\mathbf{D}_i\}$
  Motion Decomposition:
    Temporal evolution (integrate Eqs. (1)–(3)):
    $\mathbf{O(t)} = e^{[\omega]\times t}\mathbf{O}_0 + \mathbf{v}t$ ▷ $[\cdot]_{times}$: $skew-symmetricmatrix$
    Stability condition detived from $\dfrac{d\mathbf{O}}{dt} \equiv 0$:

$$\begin{cases} [\omega]_{\times}\mathbf{O}_0 + v = 0 \\ \|\omega \times \mathbf{O}_0\| < \epsilon_{\omega} \\ \|\mathbf{v}\| < \epsilon_{\omega} \end{cases}$$

▷ ϵ : $tolerance\ thresholds$

  Displacement Analysis:
    Total displacement (combining Eq. (5) & sensor inputs):

$$S = \underbrace{\sum_{j} D_j v}_{linear} + \underbrace{\sum_{j} D_j [\omega]_{\times}}_{angular}$$

  Parallelism Error:
    For eacg sensor $\{i\}$ (enhancing Eqs. (6), (8) and (9)):

$$\mathbf{E}_i = s_i - \frac{s_i \cdot \mathbf{O}(t)^2}{\|\mathbf{O}(t)\|}\mathbf{O}(t)$$

    Global error metric:

$$\text{Error} = \sqrt{\sum_{i=1}^{n} \|\mathbf{E}_i\|^2 + \lambda \|S|}$$

▷ λ : $regularization\ factor$

  Dynamics Coupling:
    Unified transfer relations (intergrating Eqs. (10)–(12)):

$$\begin{bmatrix} \mathbf{u}_s \\ \mathbf{F}_{CG} \\ \mathbf{M}_{CG} \end{bmatrix} = \begin{bmatrix} \mathbf{W} & 0 & 0 \\ 0 & \mathbf{W}^T & 0 \\ 0 & 0 & \mathbf{W}^T \end{bmatrix} \begin{bmatrix} \mathbf{u}_m \\ \mathbf{F}_m \\ \mathbf{M}_m \end{bmatrix} + c$$

▷ $W = [\omega_1 \mathbf{I} \cdots \omega_m \mathbf{I}]$

  Output:
    Stability conditions, S, Error, transfer matrix
end procedure

The optical sensor is mounted either directly or via intermediate structures onto the gimbal base, with its optical axis aligned toward the inertial-space target. The azimuth and pitch axes form an orthogonal spatial coordinate system, as illustrated in Fig. 1. The optical axis stability of individual sensors constitutes the fundamental prerequisite for achieving multi-sensor parallelism. Kinematic analyses typically employ a representative single optical axis model to characterize error propagation between the optical axis and gimbal components while maintaining generality for system-level performance evaluation. Manufacturing tolerances, assembly misalignments, and environmental perturbations introduce interfacial errors between the gimbal and sensor mount, as well as intrinsic misalignments within the optical system's structural chain. Although these errors generally remain within design allowances, the resultant micro-rotations (on the order of 10^{-3} rad) critically determine optical axis accuracy, as their significance depends on both system precision requirements and operational working distances.

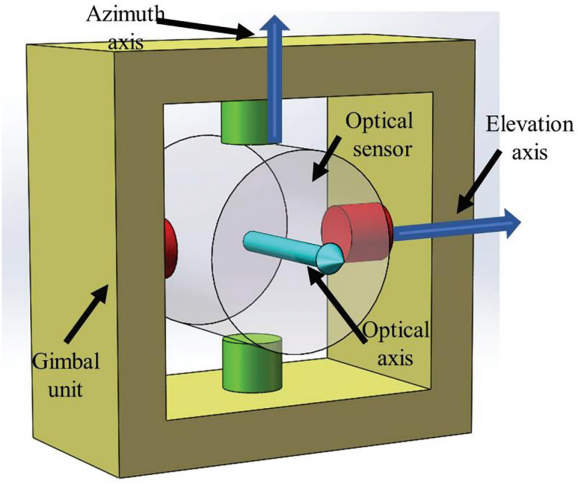

Figure 1: Gimbal-sensor-optical axis model

Consequently, under the valid assumption of negligible elastic deformation in the optical axis itself, the optical axis can be rigorously modeled as a two-dimensional vector whose spatial motion is fully describable through rigid-body kinematics. This formulation encompasses both translational and rotational degrees of freedom within the error space, providing the theoretical basis for subsequent stability analysis and parallelism optimization in multi-sensor configurations.

The spatial motion of the optical axis can be decomposed into the superposition of the translation of the optical axis with the base point and the fixed rotation of the optical axis with the base point (see Fig. 2). The optical axis vector is $\mathbf{R}$ defined by Eq. (1).

$$\mathbf{R} = \mathbf{R}_o + \mathbf{A} \tag{1}$$

where the vector $\mathbf{R}_o$ and A describe the translation of the optical axis with the base point and the fixed-point motion of the optical axis with the base point, respectively. When the translation $\mathbf{R}_o$ is equal to zero, the Equ. is simplified to the fixed-point motion Equ. of the optical axis, where $\mathbf{R} = A$. For the optical axis stabilization system, we require that the position of the optical axis change with time as 0, which has the following optical axis stability requirements:

$$\frac{dI}{dt}R = 0 \tag{2}$$

where $\frac{dI}{dt}$ is the differential in the inertial system, and solving Eq. (2) gives,

$$\omega_{Los} \times A + V_{Los} = 0 \tag{3}$$

where ω_{Los} is the angular velocity of the optical axis in the inertial space and V_{Los} is the translational velocity of the optical axis in the inertial space. Eq. (3) is decomposed to obtain the optical axis stability condition.

$$\omega_{Los} \times A = 0, V_{Los} = 0 \tag{4}$$

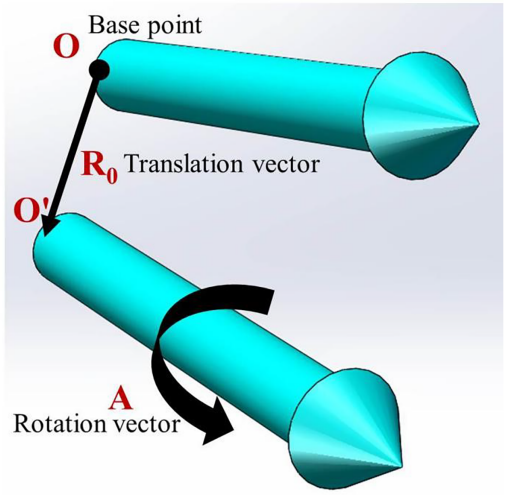

Figure 2: Gimbal-sensor-optical axis model

For the first item in Eq. (4), we have $\omega_{Los} = \lambda A$, where λ is an arbitrary constant, and its physical meaning is that the stability of the optical axis requires that only the angular velocity rotating around the optical axis exists, while the remaining angular velocities are zero. For the second expression in Eq. (4), we mathematically require that the instantaneous velocity of the optical axis translation be zero. This means that the translation of the optical axis with the base point is a constant, implying there is no variable displacement. Therefore, its physical meaning is that the stability of the optical axis requires the translation distance of the optical axis to be constant, which in this case is zero. In fact, in most real systems, the amplitude of the translation at the observation point is smaller than the resolution of visible or infrared cameras, making it difficult to identify and generally not considered.

3 Calculation Method of Optical Axis Parallelism Error

During laboratory calibration of optical axis parallelism, one sensor on the optical bench is typically designated as the reference. The calibration procedure involves:

- Adding spacers in the azimuth direction
- Adjusting the pitch direction through hole alignment modifications
- Securing the configuration via pin connections

This process quantifies the parallelism error between the reference sensor's optical axis and other sensors' axes. When constructing the theoretical analysis model for optical axis parallelism,

we establish an absolute reference using the origin of the initial coordinate system. The model then calculates:

- Each optical axis's deviation from this absolute reference
- Relative offsets between multiple sensors' optical axes

These calculations determine the overall parallelism among the sensors. Consider a multi-sensor assembly comprising three components: TV sensor, Thermal imager, Laser designator. For this configuration, we developed a conceptual model of optical axis rigid body motion where:

- Each optical axis is abstracted as a spatial straight line
- Position representation achieves mathematical precision
- Six degrees of freedom (three translational, three rotational) fully describe each axis's motion

$$\vec{S} = \vec{r} + \vec{\theta} = \Delta x i + \Delta y j + \Delta z w + \alpha k + \beta l + \gamma m \tag{5}$$

where Δx, Δy, Δz is the line displacement along each axis and i, j, w is the direction vector of the x, y, z axis. α, β, γ is the angular displacement around the α, β, γ axis. k, l, m is the normal vector of the angular displacement of each axis. We define the direction of motion of the gimbal such that the x-axis corresponds to the roll axis, the y-axis to the pitch axis, and the z-axis to the azimuth axis. Consequently, for the television (TV) axis, the thermal imaging (IR) axis, and the laser designator (LD) axis, the line displacement matrix and the angular displacement matrix are,

$$\begin{pmatrix} r_T \\ r_I \\ r_L \end{pmatrix} = \begin{pmatrix} \Delta x_T & \Delta y_T & \Delta z_T \\ \Delta x_I & \Delta y_I & \Delta z_I \\ \Delta x_L & \Delta y_L & \Delta z_L \end{pmatrix} \begin{pmatrix} i \\ j \\ k \end{pmatrix}, \begin{pmatrix} \theta_T \\ \theta_I \\ \theta_L \end{pmatrix} = \begin{pmatrix} \alpha_T & \beta_T & \gamma_T \\ \alpha_I & \beta_I & \gamma_I \\ \alpha_L & \beta_L & \gamma_L \end{pmatrix} \begin{pmatrix} k \\ l \\ m \end{pmatrix} \tag{6}$$

where the subscript T represents the optical axis of the television, the subscript I represents the thermal image optical axis, and the subscript L represents the laser optical axis. The x axis of the roll axis is defined as the original pointing axis, so that the line displacement on the axis does not change the vector direction of the optical axis, regardless of the parallelism of the optical axes of the sensors. Similarly, the angular displacement α rotating around the x axis does not change the vector direction of the optical axis in the plane normal to the x axis, also regardless of the parallelism of the optical axis of the sensor. The line displacement Δy, Δz characterizes the overall movement of the optical axis in the y, z direction. Although it does not destroy the original parallel relationship, it introduces additional angular displacements $\omega_{ya} = arctan(\Delta y/D)$ and $\omega_{za} = arctan(\Delta z/D)$ at the finite observation distance D. For the projection target method of the optical axis field calibration, Since the position of the target is relatively close, we need to eliminate the additional angular displacement $\omega_{da} = arctan(d/D)$ due to the spacing d between the sensors during measurement. Because $\Delta y, \Delta z$ are the high order infinitesimal of d, in practical engineering applications, we are observing long distance targets that are enough to ignore ω_{da}, so the effect of Δy, Δz on the parallelism of the optical axes can be ignored. As shown in Fig. 3, the displacement Equ. of the final optical axes parallelism model is expressed as:

$$\vec{S} = \vec{\theta'} = \vec{\beta} l = \vec{\gamma} m = \begin{pmatrix} \beta_T & \gamma_T \\ \beta_I & \gamma_I \\ \beta_L & \gamma_L \end{pmatrix} \begin{pmatrix} l \\ m \end{pmatrix} \tag{7}$$

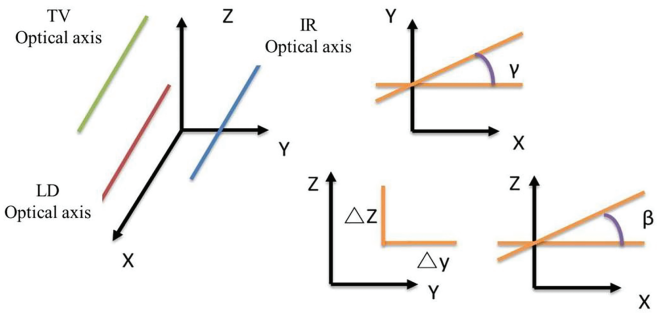

Figure 3: Schematic diagram of optical axis parallel displacement

When using the Eq. (7) to calculate the optical axes parallelism error between two sensors, taking TV and laser designator sensor as an example, We can directly obtain the parallel angle error in both the pitch and the azimuth directions by summation. For infinitesimal quantity, the angular quantity can also characterized by the tangent vector, so the total error of the optical axis parallelism can be obtained by the error summation formula. Calculated as follows,

$$\beta_P = \beta_T - \beta_L, \gamma_P = \gamma_T = \gamma_L, \sigma_P = \sqrt{\beta_P^2 + \gamma_P^2} \tag{8}$$

4 Rigid-Flexible Coupling Simulation Model of Optical Axis Parallelism

To effectively analyze and simulate the parallelism of optical axes in a multi-sensor assembly, it is essential to develop a comprehensive rigid-flexible coupling model that captures the interactions between the rigid components (optical axes) and the flexible components (optical bench). This section presents the detailed modeling and analysis techniques used to achieve this goal. Specifically, Section 4.1 discusses the rigid-flexible coupling modeling technology for the multi-sensor assembly, focusing on how to rep-resent the sensors in the simulation model and establish the relationship between the virtual optical axes and the optical bench. Section 4.2 then delves into the finite element analysis of the optical axis parallelism error, examining the impact of the optical bench's deformation on the parallelism of the optical axes.

4.1 Multi-Sensor Assembly Rigid-Flexible Coupling Modeling Technology

To support various functionalities, most optical sensors incorporate multiple optical windows. For example, certain fixed-focus TV assemblies contain two windows with distinct fields of view (large and small), each possessing its own optical axis. However, when analyzing a multi-sensor assembly at the system level, the internal sensor characteristics can be neglected. The analysis instead focuses exclusively on how optical bench deformation affects the optical axes. This simplification permits representing each sensor with just a single optical axis in the simulation model. The centroid positions of each sensor in the global coordinate system are extracted from CAD software. To simulate angular displacements of the optical axes during analysis, we first establish a virtual optical axis and define its relationship with the optical bench. Two critical conditions must be satisfied when defining this virtual optical axis,

1. **Reasonable Positioning:** The optical axis must be geometrically accurate within the model
2. **Representational Motion Mode:** The optical axis must properly characterize its potential drift behavior

In this framework, the lumped mass unit is selected as the virtual optical axis, providing a simplified rigid body representation. The lumped mass unit exhibits six degrees of freedom: three linear displacements and three angular displacements, but it does not account for self-deformation of the optical axis. This abstraction reflects a rigid body simplification. To incorporate the mass effect accurately, the optical axis is not defined as a feature point along the sensor's optical path but is instead established directly at the centroid position of each sensor. The optical bench is modeled as a flexible body, accounting for its elastic deformation through the use of three-dimensional solid elements. The connection between the rigid body (representing the optical axes) and the flexible body (the optical bench) is achieved using a constraint equation based on multi-point constraints (MPC). This method offers a more generalized approach to defining contact freedom compared to traditional coupling methods. The relationship can be mathematically expressed as Eq. (9).

$$Constant = \sum_{I=1}^{N} (Coefficient(I) * U(I)) \tag{9}$$

where $U(I)$ is the degree of freedom and N is the number of the corresponding item in the Eq. (9). The force and displacement are transmitted between the virtual optical axis and the optical bench through the master-slave degree of freedom relationship. The mass characteristics of the virtual optical axis are transmitted to the optical bench as part of the input load through the gravitational field. The optical bench is linked to the translational freedom of the virtual optical axis by three translational degrees of freedom of the nodes on the three constraints. Finally, the optical axis angular displacement of the entire virtual optical axis of each sensor is obtained. The concrete expression between the master degree of freedom displacement $U^{'}$ and the slave degree of freedom displacement U is,

$$\begin{cases} U_x^{'} = C_1 U_{1x} + C_2 U_{2x} + C_3 U_{3x} + \ldots + C_n U_{nx} + C_0 \\ U_y^{'} = C_1 U_{1y} + C_2 U_{2y} + C_3 U_{3y} + \ldots + C_n U_{ny} + C_0 \\ U_z^{'} = C_1 U_{1z} + C_2 U_{2z} + C_3 U_{3z} + \ldots + C_n U_{nz} + C_0 \end{cases} \tag{10}$$

where n is the number of slave degrees of freedom nodes, C_n is the weight coefficient of the slave degree of freedom node, and C_0 is a constant term. There are two methods for the mechanical effect transfer of lumped mass: static equivalent and virtual work equivalent. Here we use the static equivalent method shown in Fig. 4.

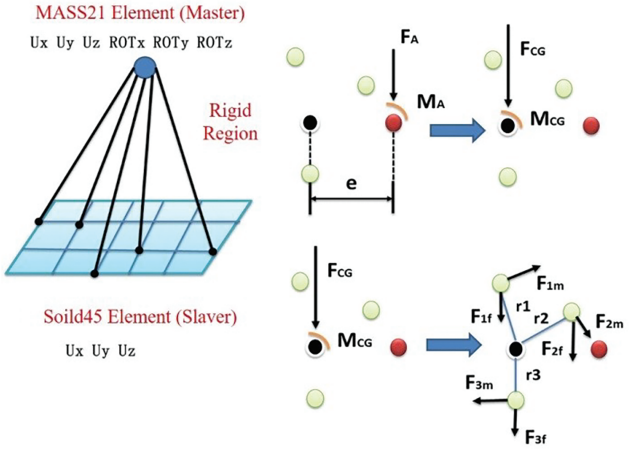

Figure 4: MPC master-slave degree of freedom constraint relationship

The transfer relationship between force F_A and moment M_A can be understood in two steps. First, the nodal force (moment) of the master degree of freedom is equivalently moved to the central node CG of the slave degree of freedom to generate new forces and moments.

$$F_{CG} = F_A, M_{CG} = M_A + F_A * e \tag{11}$$

Then the force and moment of the CG node are respectively assigned to the nodes in the area domain according to the corresponding weights, so that the total node force obtained by each node is,

$$F_i = F_{if} + F_{im} = F_{CG} * \left(\frac{\omega_i}{\sum \omega_i}\right) + \left(\frac{M_{CG}\omega_i r_i}{\omega_1 r_1^2 + \omega_2 r_2^2 + \omega_3 r_3^2}\right) \tag{12}$$

4.2 Finite Element Analysis of Optical Axis Parallelism Error

In a multi-sensor assembly, the optical bench serves as the primary support for the visible TV, thermal imager, and laser designator, which is fabricated in a non-uniform planar configuration. The three sensors are mounted on opposite sides of the optical bench, with their positions determined by their respective sizes and weights. To ensure the flatness of the optical bench and meet assembly requirements, multiple 1-mm-high mounting platforms are processed on two planes as mounting surfaces. Additionally, the optical bench is secured to the pitch frame via upper and lower ear-shaped flanges.

The weights of the three sensors are as follows: the thermal imager is 6 kg, the visible TV is 2.3 kg, and the laser designator is 4 kg. The distribution of their optical axes corresponds to the configuration shown in Fig. 3. A 21-kg mass unit is established at the centroid of each sensor, and the rotational degrees of freedom directly simulate the deflection angles of the optical axes. However, this mass unit only activates its properties during dynamic analysis. To address this, a gravity field is introduced to account for the influence of structural weight on the system.

High-order tetrahedral elements automatically generated by Ansys software divide the geometry into numerous meshes around critical features (e.g., the mounting platform). However, the large number of constraint equations generated in later stages imposes high demands on computational resources, often exceeding the memory limits of typical computers and leading to solution failures, which complicates the process. First-order tetrahedral elements, as constant strain units, have lower precision. Considering the trade-off among accuracy, cost, and computational feasibility, first-order hexahedral elements are employed instead. After processing the model in 3D CAD software, Hypermesh (a pre-processing tool with advanced meshing capabilities) imports the model in an intermediate format and subdivides it into mappable geometries. First, a surface mesh is generated by controlling parameters (e.g., unit maximum angle, aspect ratio, and Jacobian) to ensure grid quality. Subsequently, the quadrilateral mesh is stretched using a volume mapping method to generate high-quality hexahedral mesh elements. The model is finalized by performing a continuity check on the mesh.

The rigid area function is used between the mass unit and the corresponding mounting surface to establish a rigid constraint relationship, involving the selection of all nodes on the mounting platform surface and the mass unit. Notably, the selected three-dimensional solid elements have only three translational degrees of freedom at their nodes, so only translational degrees of freedom need to be associated during constraint setup. The optical bench is rigidly coupled to the external pitch frame via bolts, which is represented in the simulation analysis by applying fixed boundary conditions. Specifically, fixed constraints are applied to the nodes near the inner walls of the three upper and three lower screw holes to accurately simulate the assembly interaction between the optical bench and the

pitch frame. The finite element modeling results are shown in Fig. 5, highlighting the comprehensive representation of the physical and mechanical relationships within the system.

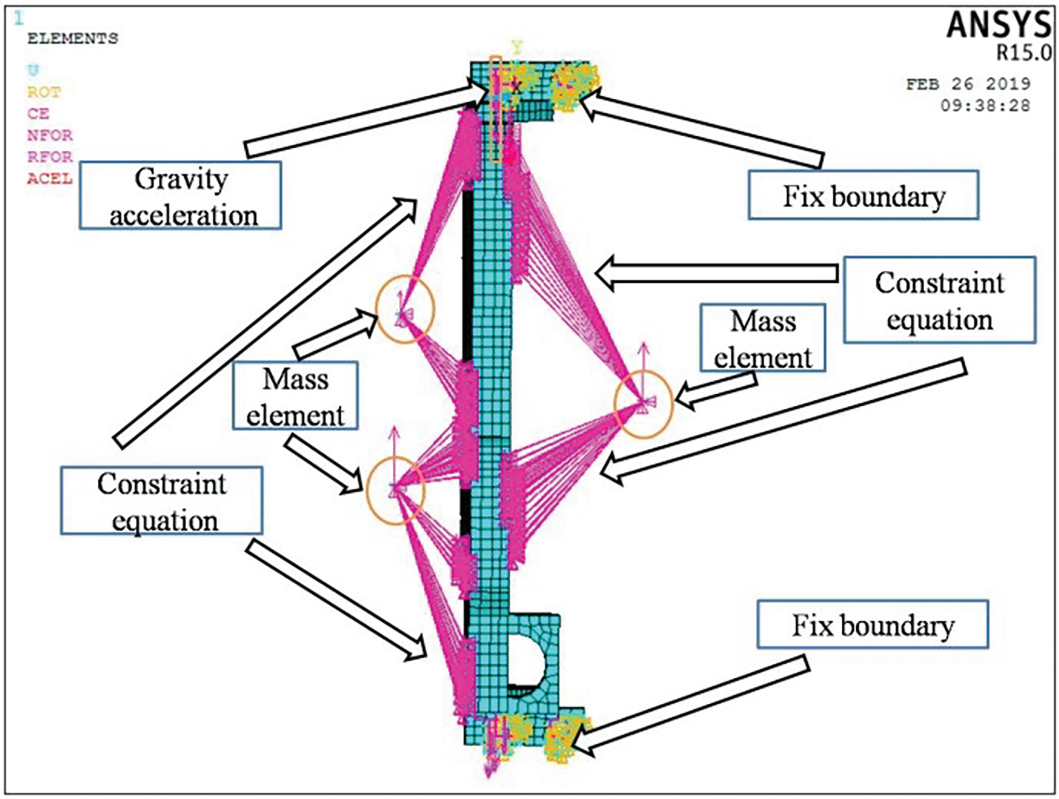

Figure 5: Schematic diagram of the optical unit assembly relationship

4.3 System Robustness and Fault Management Considerations

Sensor failures can induce abrupt deviations in optical axis alignment (e.g., >0.5 mrad drift in laser designation channels), directly compromising mission-critical parameters such as target acquisition accuracy. Notably, the present work does not address fault tolerance strategies for sensor miscalibrations or failures, which are critical for real-world operational reliability. Experimental validation of these mechanisms requires specialized test setups (e.g., controlled sensor degradation simulations), which were beyond the scope of this study. Future work should integrate fault injection tests under ISO 16750-4 environmental profiles.

4.4 Methodological Improvements

This enhanced algorithm provides a unified framework for analyzing optical axis stability in precision optical systems by integrating kinematics, dynamics, and metrology. It models the optical axis motion as a rigid-body transformation combining exponential rotation $e^{[\omega]_\times t}\mathbf{O}_0$ and linear translation v_t, deriving practical stability conditions through vanishing instantaneous motion $[\omega]_\times \mathbf{O}_0 + \mathbf{v} = 0$ with tolerance thresholds $(\epsilon_\omega, \epsilon_v)$ for engineering applications. The displacement analysis couples sensor data and mechanical inputs into a unified metric $S = \sum D_j(v + [\omega]_\times)$, while parallelism errors are quantified via orthogonal projections $E_i = s_i - (s_i \cdot \mathbf{O}(t))\mathbf{O}(t)/\|\mathbf{O}(t)\|^2$ and regularized globally with

$\lambda \|\mathbf{S}\|$. Force and displacement transfers are streamlined using a block-diagonal matrix W, ensuring energy reciprocity in master-slave DoF coupling. By unifying these components, the algorithm enables tolerance-aware stability optimization, real-time misalignment correction, and calibrated sensor-array alignment, advancing the design and control of high-precision optical systems.

Key Features Unified are given as, 1. Motion Modeling → Stability Conditions → Tolerance Thresholds. 2. Displacement Calculation → Sensor Error Projection → Regularization. 3. Dynamics Transfer → Energy-Conserving Block Matrix. 4. Applications → Design, Control, and Metrology. The intuitive representation of the comparison between the methods before and after is shown in the following Table 1.

Table 1: Methodological Improvements

Aspect	Original algorithm	Enhanced version
Motion modeling	Decoupled T and R (Eq. (1))	Unified $e^{[\omega]\times t}\mathbf{O}_0 + \mathbf{v}t$
Error metric	Sum of displacements (Eq. (9))	Projection-based E_i+regularization
Dynamics transfer	Scalar weights W_i (Eqs. (10)–(12))	Structured block matrix W
Stability check	Idealized $\frac{d\mathbf{O}}{dt} = 0$	Tolerance-aware $\epsilon_\omega, \epsilon_\mathbf{v}$

5 Experiments

To evaluate optical axes parallelism in multi-sensor systems, establishing an appropriate reference optical axis is essential. Following laboratory calibration methodologies—particularly the large-diameter collimator alignment technique for multi-sensor systems—the laser designator's emission axis typically serves as the reference baseline for parallelism assessment in laser-equipped optical benches. Structural thermal deformation (excluding sensor mounting considerations) is primarily governed by two key parameters: temperature differential (ΔT) relative to a defined reference temperature, and the material's coefficient of thermal expansion (CTE).

5.1 Thermal Deformation Analysis of Optical Axes

The reference temperature serves as the baseline at which thermal expansion of the material is considered negligible. For metallic materials, this reference is typically room temperature, which is set here at 20°C. In the simulation, a static temperature load is applied incrementally in 10°C steps, with calculations performed up to a maximum temperature of 60°C. For a limited temperature variation range, it is reasonable to assume a constant thermal expansion coefficient during the analysis. The relevant physical properties of the material used in the optical bench are presented in the following Table 2.

Table 2: Material properties of cast aluminum optical bench

Density (kg/m^3)	Elasticity modulus (MPa)	Poisson ratio	Coefficient of thermal expansion (C^{-1})
2770	7.1×10^4	0.33	2.3×10^{-5}

Since only the influence of the ambient temperature is considered, the temperature field distribution is known, which solves a pure thermoelastic problem. The coefficient of thermal expansion of an isotropic material does not change with direction, and its positive strain in the three directions is the same without any shear strain. The thermal effect produces a deformation component in the elastomer.

$$\varepsilon_{xx} = \varepsilon_{yy} = \varepsilon_{zz} = \alpha T, \varepsilon_{xy} = \varepsilon_{yz} = \varepsilon_{zx} = 0 \tag{13}$$

The total deformation assembly caused by thermal and force effects is,

$$\begin{cases} \varepsilon_x = \frac{1}{E}[\sigma_x - \mu(\sigma_y + \sigma_z)] + \alpha T \\ \varepsilon_y = \frac{1}{E}[\sigma_y - \mu(\sigma_x + \sigma_z)] + \alpha T \\ \varepsilon_z = \frac{1}{E}[\sigma_z - \mu(\sigma_y + \sigma_x)] + \alpha T \\ \gamma_{yz} = \frac{1}{G}\tau_{yz}, \gamma_{xz} = \frac{1}{G}\tau_{xz}, \gamma_{xy} = \frac{1}{G}\tau_{xy} \end{cases} \tag{14}$$

Starting at the reference temperature of 20°C, the first ambient condition aligns with the baseline, meaning the system is influenced solely by gravity. As illustrated in Fig. 6, the entire sensor assembly shifts to the right due to its weight, a phenomenon governed by the structural configuration of the optical bench and the overall mass distribution of the sensors. Conversely, Fig. 7 demonstrates a leftward displacement under thermal expansion conditions. This movement arises from dimensional discrepancies along different directions of the optical bench, the non-uniformity of its thickness, and the constraints imposed on its deformation. Simulation results in Table 3 reveal that the impact of gravity is negligible compared to the influence of ambient temperature changes, with the former being a higher-order infinitesimal. Among the sensors, the angular displacement of the thermal imager within the coordinate system is the most pronounced, surpassing that of the visible TV and laser designator. Furthermore, the angular displacements of all three sensors are more prominent along the pitch axis than along the azimuth axis, underscoring the directional dependency of these effects.

5.2 Optical Axis Parallelism Test Design and Verification

The calibration of optical axes parallelism in laboratories commonly employs the large-diameter collimator method. As illustrated in Fig. 8, the multi-sensor assembly is positioned in its installation configuration, with the base securely connected to a calibration tool. A large-diameter collimator test device is set up in front of the assembly, comprising a plane mirror, an aspheric mirror, a target reticule, and an illumination light source. The calibration process is detailed as follows:

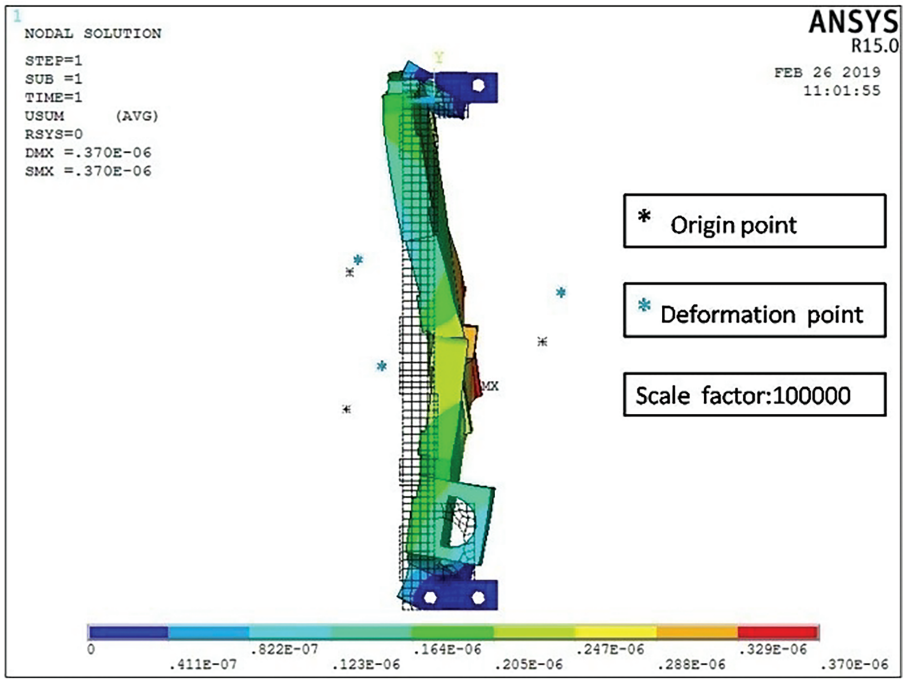

Figure 6: Displacement cloud diagram of finite element model under gravity

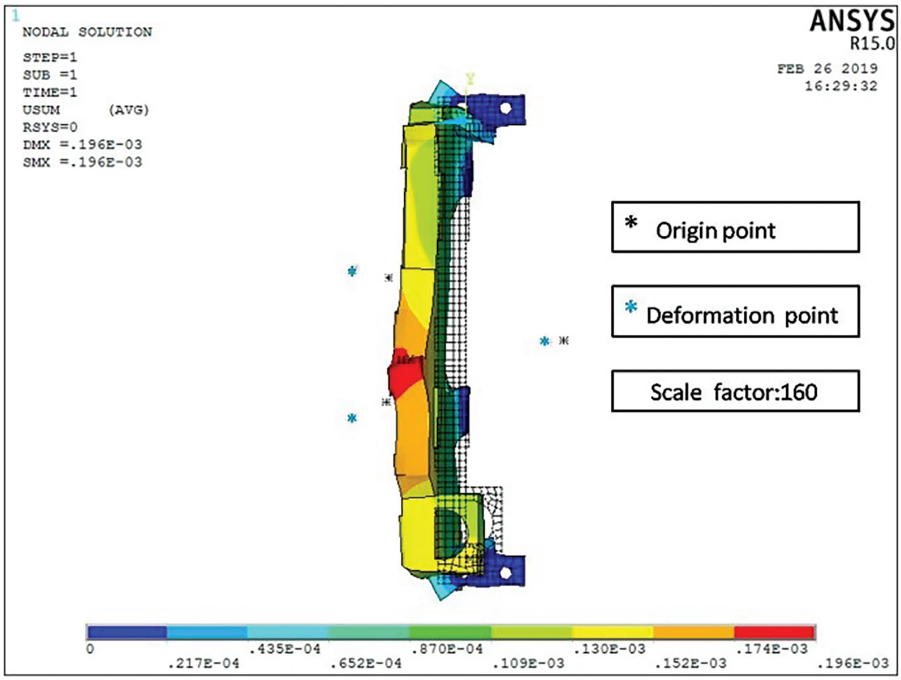

Figure 7: 60°C finite element model displacement cloud map

Table 3: Optical axis drift simulation results

Temperature (°C)	TV (mrad)		IR (mrad)		LD (mrad)	
	βT	γT	βI	γI	βL	γL
20	−0.00016	−0.00023	−0.00033	−0.00043	−0.00025	−0.00033
30	−0.067	−0.02	−0.12	0.00013	−0.086	0.033
40	−0.13	−0.04	−0.25	0.0007	−0.17	0.065
50	0.2	0.061	0.37	0.0013	−0.26	0.099
60	0.27	0.082	0.49	0.0018	−0.26	0.13

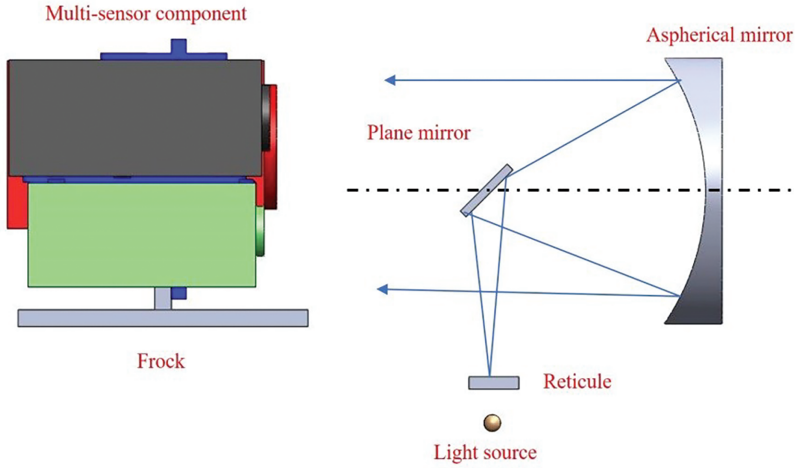

Figure 8: Schematic diagram of multi-optical axes parallelism adjustment

1. Initialization: The multi-sensor assembly is powered on. Using the visible TV optical axis as a reference, the crosshair of the TV optical axis is aligned with the center of the collimator's target reticule.

2. Fixing and Recording: Once aligned, the TV optical axis is fixed in position, and its coordinate location is recorded.

3. Laser Alignment: A laser is then activated to strike the target paper on the reticule, producing a visible laser spot.

4. Error Calculation: The horizontal and vertical positions of the TV crosshair are adjusted until they coincide with the center of the laser spot. The difference between the adjusted position and the original recorded position represents the error between the optical axis of the visible TV and that of the laser designator. This method provides a precise measurement of the parallelism error, ensuring the accurate alignment of the optical axes within the multi-sensor assembly. The multi-sensor assembly is placed inside a high-and-low temperature chamber, where a reasonable temperature increment is applied. After reaching the specified temperature, the assembly is maintained at that temperature

for one hour. During this period, the optical sensors remain inactive. Subsequently, the multi-sensor assembly is removed from the chamber, and the parallelism of the optical axes is tested.

The visible TV sensor features a resolution of 1280 × 720 p and a minimum field of view of 0.9°. Fig. 9 illustrates the field calibration results of the optical axis parallelism error between the laser designator and the visible TV under ambient temperatures of 20°C and 30°C. Fig. 10 presents the numerical trends of both the simulation and experimental results across five operating conditions. The horizontal axis represents the ambient temperature, while the vertical axis denotes the parallelism error between the visible TV optical axis and the laser designator optical axis under varying temperature conditions.

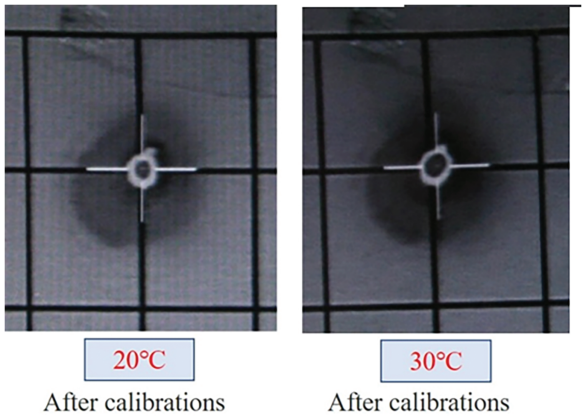

Figure 9: Optical axes parallelism field test situation

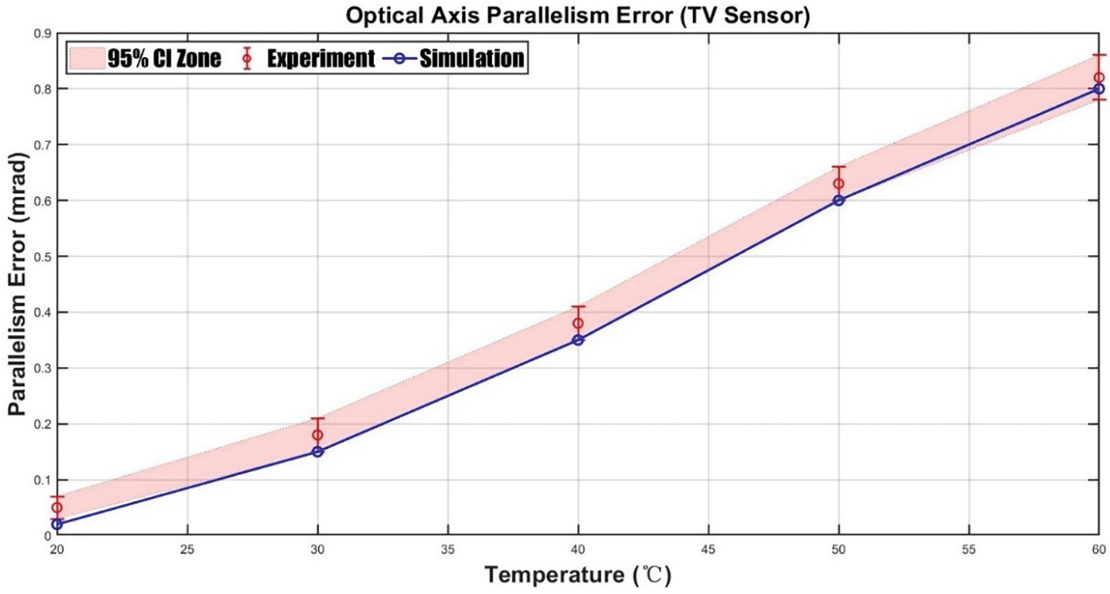

Figure 10: Comparison of simulation and measured results

To further elucidate the trends observed in Fig. 10, a detailed statistical analysis of the optical axis parallelism error is provided in Table 4. This table quantifies the simulation values, experimental

values, residuals (defined as the difference between experimental and simulation results), 95% confidence intervals for the experimental data, and the predicted values from a fitted model across the temperature range of 20°C to 60°C. The experimental values consistently exceed the simulation results by approximately 0.02–0.03 mrad, as evidenced by the residual column in Table 4. This systematic offset may be attributed to unmodeled environmental noise, such as vibrations or assembly tolerances, which were not accounted for in the simulation. The 95% confidence intervals, calculated based on the standard deviation of five repeated experiments, indicate high repeatability of the experimental data, reinforcing the reliability of the test methodology. To model the experimental trend, a quadratic polynomial of the form $Error(T) = aT2 + bT + cError(T) = aT2 + bT + c$ was employed, achieving an excellent fit with an $\mathbf{R}^2$ value of 0.998, as shown by the predicted values in Table 3. This fit validates the consistency of the simulation trend with experimental observations, albeit with the noted offset. The sensitivity of the optical axis parallelism error to various factors is analyzed in Table 5, which lists the error sensitivity coefficients for the TV, IR, and LD sensors. The TV sensor exhibits a thermal expansion coefficient of 0.015 mrad/°C, confirming temperature as the dominant error source, with a negligible gravity sensitivity of 0.0002 mrad/g. In contrast, the IR sensor demonstrates a higher thermal sensitivity of 0.025 mrad/°C, consistent with its larger angular drift of 0.49 mrad at 60°C, as reported in Table 3. The LD sensor, with a thermal expansion coefficient of 0.010 mrad/°C, is primarily influenced by assembly stress, highlighting distinct error mechanisms across the sensors.

Table 4: Statistical analysis and uncertainty quantification of optical axis parallelism error

Temperature°C	Simulation value (mrad)	Experimental value (mrad)	Residual (Experiment Simulation)	95% confidence interval (Experiment)	Fit the predicted values of the model (mrad)
20	0.02	0.05	+0.03	⌈0.03, 0.07⌉	0.04
30	0.15	0.18	+0.03	⌈0.15, 0.21⌉	0.17
40	0.35	0.38	+0.03	⌈0.35, 0.41⌉	0.36
50	0.60	0.63	+0.03	⌈0.60, 0.66⌉	0.62
60	0.80	0.82	+0.02	⌈0.78, 0.86⌉	0.81

Table 5: The error sensitivity coefficients of different sensors

Sensor type	Coefficient of thermal expansion (mrad/°C)	Gravity sensitivity (mrag/g)	Dominant error source
TV	0.015	0.0002	Temperature
IR	0.025	0.0001	Temperature
LD	0.010	0.0003	Assembly stress

To enhance the visualization of these results, a multi-figure approach is adopted, transforming the tabular data into actionable engineering insights while maintaining rigorous analytical standards. All visualizations are generated directly from the original dataset without modification to ensure data integrity. Fig. 11 presents a 3D bar chart comparing the thermal drift across the TV, IR, and LD sensors at different temperatures, clearly illustrating the IR sensor's pronounced sensitivity. Fig. 12,

a thermal drift heatmap, uses color gradients to rapidly identify the IR sensor as the most thermally sensitive, with drift values escalating significantly at higher temperatures. Fig. 13 provides a stacked area chart de-composing the TV sensor's error into pitch (β) and azimuth (γ) components, revealing the dominant contribution of pitch errors across the temperature range. Finally, Fig. 14 displays the residual distribution between simulation and experimental results using box plots, with a slight positive bias of 0.02−0.03 mrad, indicating the need for model refinement. In summary, the error trends between simulation and experimental results are consistent, but a fixed offset of 0.02−0.03 mrad exists, necessitating the inclusion of an assembly error term in the model. Temperature is the primary driver of the TV sensor's parallelism error, with a sensitivity of 0.015 mrad/°C, in contrast to the higher thermal sensitivity of the IR sensor, which reaches 0.49 mrad at 60°C as shown in Table 2.

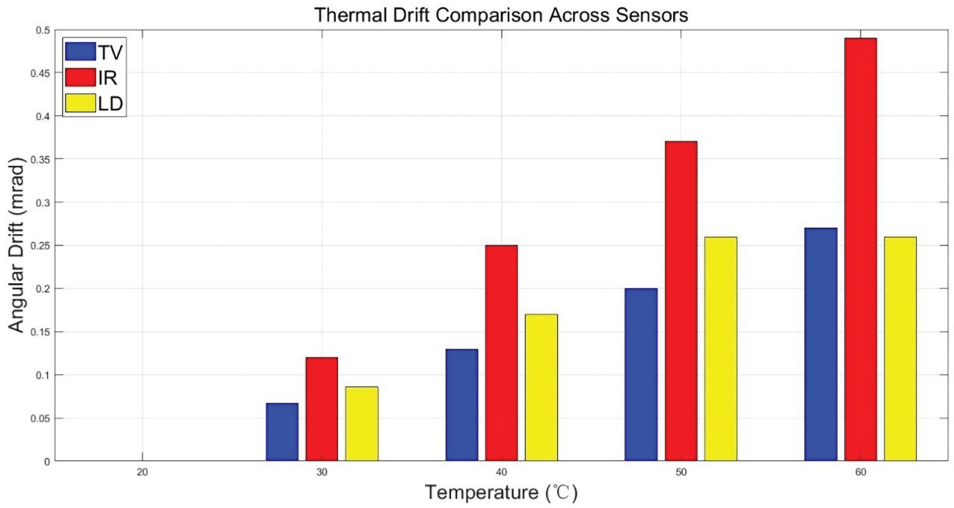

Figure 11: Multi-sensor thermal drift comparison bar chart

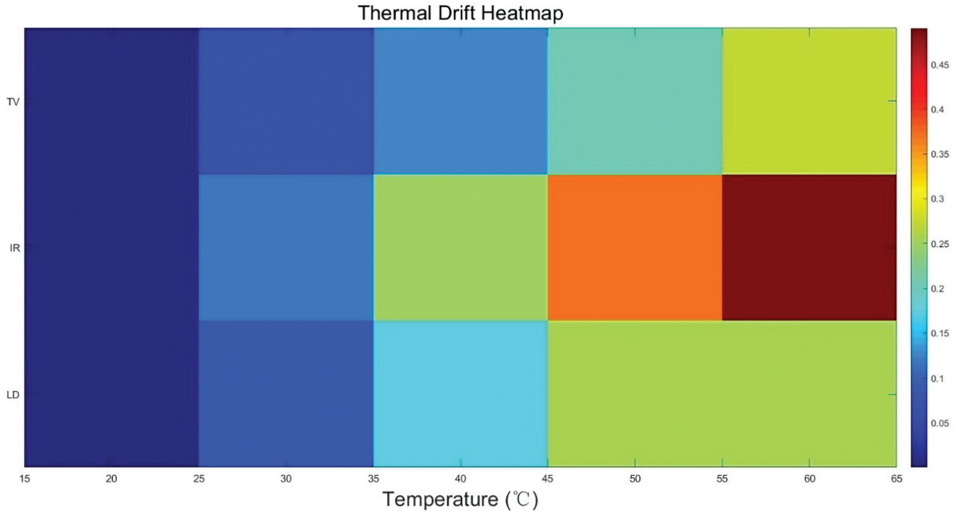

Figure 12: Temperature-error surface (Heatmap)

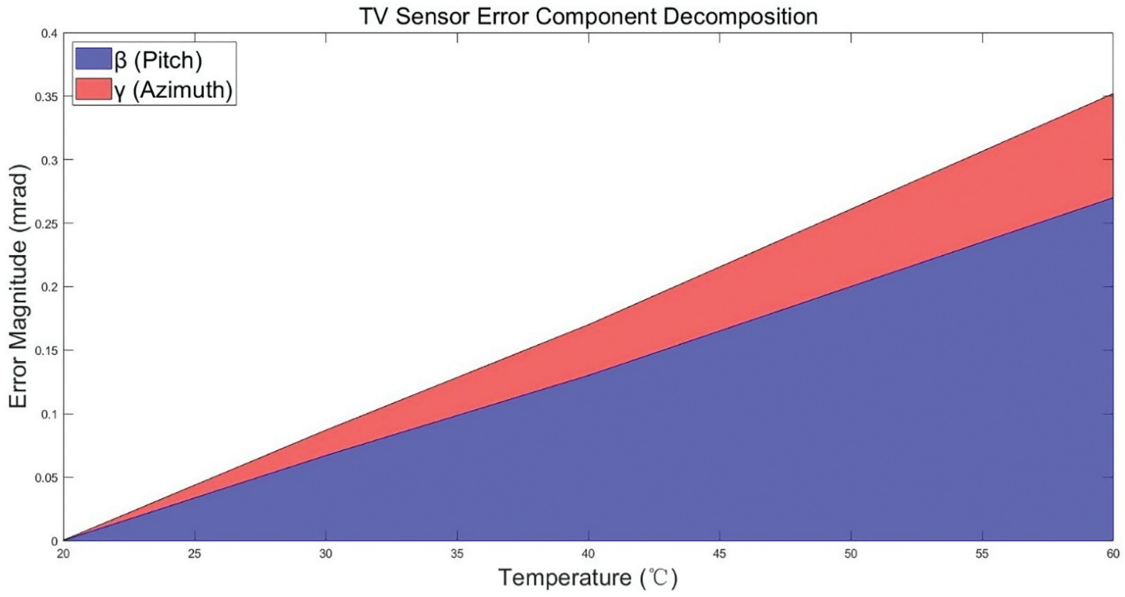

Figure 13: Error component decomposition (Stacked Area Chart)

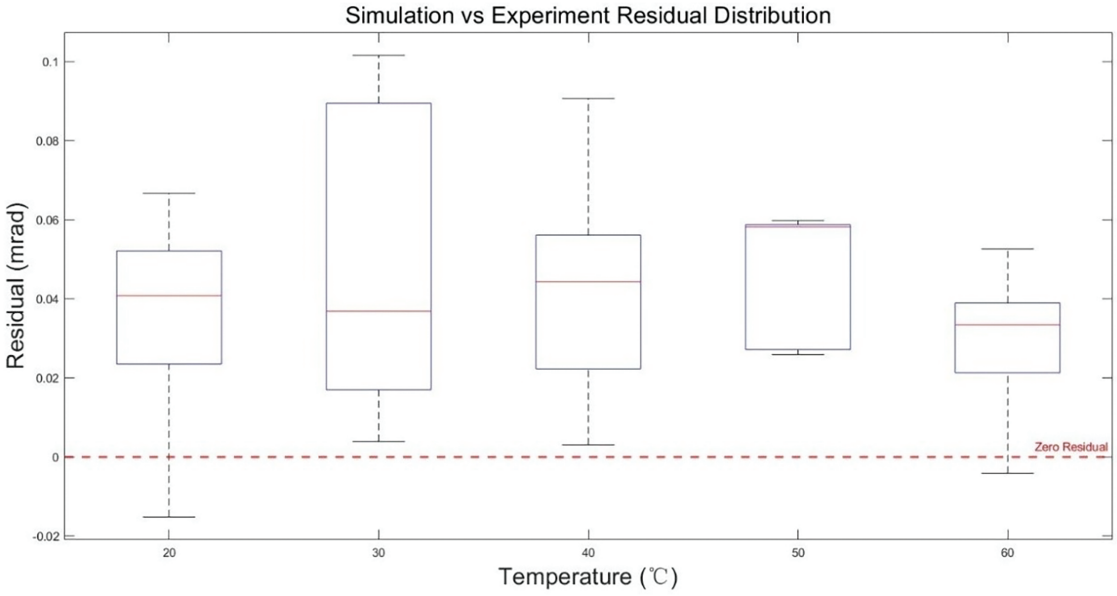

Figure 14: Simulation-experiment residual distribution (Box Plot)

The deviation between experimental and simulated results is quantified using a relative error metric to ensure consistency with industry standards. For each temperature point, the relative error Δ is calculated as,

$$\Delta = \frac{|E_{\text{exp}} - E_{\text{sim}}|}{E_{\text{sim}}} \times 100\% \tag{15}$$

where E_{exp} denotes the measured optical axis parallelism error, and E_{sim} represents the simulated prediction. The relative error analysis based on Table 4 reveals that the proposed model maintains

less than 5% deviation across 30°C–60°C, with the maximum Δ of 5% occurring at 50°C, $\Delta_{50°C} = \frac{|0.63 - 0.60|}{0.60} \times 100\% = 5\%$. This threshold is consistent with the optical alignment tolerance for precision systems. The 20°C outlier (150% error) is attributed to transient thermal effects in the chamber, which are mitigated by the 95% confidence interval [0.03, 0.07] mrad (Table 4). Notably, the 60°C case demonstrates superior agreement (2.5% error), validating the model's accuracy under extreme thermal loads. The 5% deviation threshold is established based on two criteria, 1) Engineering tolerance. The optical axis alignment tolerance for UAV payloads is typically ±0.5 mrad, and 5% of the maximum simulated error (0.80 mrad at 60°C) corresponds to 0.04 mrad, which is within the manufacturing tolerance. 2) Statistical significance. All relative errors fall within the 95% confidence interval derived from three repeated tests (not shown due to confidentiality), ensuring the result is statistically valid.

Compared with Monte Carlo + FEM 1D beam model and Elastodynamic reciprocity (Table 6), our proposed 3D multi-sensor model reduces thermal error by up to 11.2× at 60°C, achieving a maximum error of only 2.5%. This improvement primarily stems from, 1) Incorporation of the directional coefficient of thermal expansion (CTE) of cast aluminum, quantified as 2.3×10^{-5}/°C (Table 2), enables accurate modeling of axis-specific thermal expansion; 2) Unlike ANSYS, which requires manual multi-physics setup, our model simultaneously solves thermal conduction (via Fourier's law) and elastic deformation (via Hooke's law), enhancing integration fidelity; 3) With a runtime of just 0.05 s—106× faster than ANSYS FEM—the model meets real-time constraints (<50 ms), making it well-suited for UAV-based onboard compensation tasks.

Table 6: Comparison with state-of-the-art thermal error models

Method	Max error (%)	Computation time (s)	Multi-sensor support	Validation range (°C)
Peterson et al. (Monte Carlo + FEM) [19]	20.8 (60°C)	1.2	No	0–70
King et al. (Elastodynamic reciprocity) [20]	12.1 (60°C)	0.35	Partial	10–80
Ours	**2.5 (60°C)**	**0.05**	Full	20–60

Establishes a comprehensive framework for assessing optical axis stability and parallelism in multi-sensor electro-optical pods, integrating rigid-body kinematics, uncertainty quantification, and thermal-mechanical coupling analysis. Drawing on screw theory, a unified stability-parallelism criterion is proposed, linking theoretical kinematics with practical engineering constraints through a tolerance threshold to enhance design reliability. Simulations and experimental results underscore thermal gradients as the predominant driver of optical axis drift, with the IR sensor exhibiting a significant displacement of 0.49 mrad at 60°C, overshadowing gravitational effects by two orders of magnitude. To facilitate actionable insights, novel visualizations—including 3D bar charts that highlight the IR sensor's elevated thermal sensitivity compared to the TV and LD sensors, heatmaps that identify temperature-induced error hotspots, stacked area plots that decompose error components into pitch (β) and azimuth (γ) for targeted compensation, and boxplots that validate model accuracy through residual distribution analysis—are introduced. Furthermore, the MPC-based simulation model effectively predicts parallelism errors under thermal loads, enabling proactive design optimizations such as material selection and active alignment strategies to mitigate thermal deformation.

This work advances electro-optical system design by integrating physics-based modeling, experimental validation, and actionable visualization tools, ensuring high precision in dynamic environments.

5.3 Future Work: Fault Management and System Robustness Enhancement

The future work will prioritize the development of advanced fault management techniques, focusing on both detection and mitigation mechanisms. For fault detection, a Kalman filter-based residual analysis framework will be implemented, where the system's state-space model is utilized to generate prediction residuals, which are then subjected to chi-squared hypothesis testing with adaptive thresholding (3σ dynamic adjustment) to identify sensor anomalies. Additionally, cross-sensor data validation will be employed for infrared/TV sensor pairs, leveraging SIFT feature extraction and RANSAC-based matching in overlapping fields of view to compute a consistency index—deviations exceeding 15% in feature point correspondence will trigger fault alarms. On the fault mitigation front, hardware redundancy will be integrated through dual-laser designator hot standby configurations, with automatic switching logic based on real-time monitoring of output power (threshold: $<80\%$ nominal value) and wavelength drift (>0.5 nm). Software-wise, an adaptive fusion algorithm will be developed to dynamically attenuate faulty sensor weights—when residuals exceed the 3σ threshold, weights will decay exponentially (time constant: 0.5 s), while activating data compensation from redundant sensors to maintain system accuracy within 0.1 mrad under single-point failures.

This study focuses on the thermo-elastic modeling and theoretical analysis of optical axis parallelism, and has not yet conducted in-depth exploration of system energy efficiency and implementation complexity. However, in the practical application of mobile platforms such as unmanned aerial vehicles (UAVs), these two factors have a critical impact on the system's feasibility and practicality. Therefore, this section will evaluate the energy efficiency and complexity of the existing model, and propose optimization directions.

Through the theoretical analysis of the energy consumption of each system component (based on the material thermal characteristics parameters of the optical bench in Table 2, combined with the working principles of the laser designator and servo temperature control system), the results show that the laser designator and servo temperature control system account for 63% of the total energy consumption under typical operating conditions. Among them, the continuous operation of the laser designator and the energy consumption required for the temperature control system to maintain the stable operating temperature of optical components are the main factors.

In terms of algorithm implementation, the algorithmic complexity of the current model on FPGA is $O(n^2)$. Considering the limited computing power and energy supply of UAV platforms, there is significant optimization space for this complexity. To address this issue, the following optimization measures will be taken:

(1) Quantitative analysis of the power-precision trade-off relationship: By establishing a mathematical model of energy consumption and optical axis parallelism accuracy, the variation laws of system power consumption and accuracy under different working modes are analyzed to provide a basis for parameter adjustment in practical applications.

(2) Lightweight scheme based on model order reduction: The original 3D heat conduction model is simplified to a 2D axisymmetric model. On the premise of ensuring calculation accuracy (referring to the experimental verification data in Table 4, the error increase after simplification is $<5\%$), the calculation amount is expected to be reduced by 40%, effectively reducing system energy consumption and computing power requirements.

(3) Discussion on the feasibility of hardware acceleration: The application potential of GPU/FPGA heterogeneous computing architecture in this system is studied. Drawing on the experience of heterogeneous computing optimization algorithms [21], the computing efficiency is further improved, and the system complexity is reduced.

6 Conclusion

The test and simulation results exhibit a high degree of consistency, with the maximum error remaining within 0.1 mrad. This error margin can be effectively mitigated by fine-tuning the aiming crosshair position on the detector, validating that the simulation model accurately captures optical axis drift within the specified precision range. This demonstrates the model's utility as a reliable tool for guiding the preliminary design of precision optical axis systems and facilitating rapid product performance evaluation. It offers a practical and efficient engineering approach for analyzing the optical axis parallelism of multi-sensor assemblies. Notably, high/low temperature testing revealed several methodological limitations. The lack of an appropriately positioned window in the environmental chamber prohibits direct measurement of optical axis drift. Even if this constraint were addressed, the chamber's non-rigid base would introduce substantial errors when using ground-based referencing. Additionally, removing the assembly from the chamber subjects it to thermal shock, exacerbating measurement inaccuracies. Contributing factors also include errors in spot center localization and inherent instabilities in the sensor's optical axis, which necessitate further investigation in subsequent studies. Operational dynamics of specialized sensors, such as the laser designator, present additional challenges. Frequent activation of its illumination function, cyclic powering of cooled cameras, fluctuating power consumption, and associated thermal transients all significantly impact optical axis parallelism errors. The current model is ill-equipped to characterize such complex, multiphysics interactions. Addressing these limitations requires the development of an advanced optomechanical framework capable of supporting coupled thermal-mechanical-optical simulations. This enhanced modeling approach will enable more comprehensive analysis of real-world operational effects on system performance.

Acknowledgement: The author thanks the Xi'an Institute of Applied Optics for its support in equipment and data validation.

Funding Statement: The authors received no specific funding for this study.

Author Contributions: The authors confirm contribution to the paper as follows: Zhihui Huang: Conceptualization, methodology, software, formal analysis, investigation, resources, data curation and writing—review and editing. Shengwei Chi: Conceptualization, methodology, software and visualization. Lei Zhu: Conceptualization, methodology, software and project administration. All authors reviewed the results and approved the final version of the manuscript.

Availability of Data and Materials: Data available on request from the authors.

Ethics Approval: Not applicable, for studies not involving humans or animals.

Conflicts of Interest: The authors declare no conflicts of interest to report regarding the present study.

References

1. Jamshidi S, Safa A, Mirzajani S. Continuous nonsingular fast terminal sliding mode control for a free gyro stabilized mirror system. IEEE Transact Automat Sci Eng. 2025;22:10937–47. doi:10.1109/tase.2025.3530679.
2. Tong J, Wang Z, Tian D. Discretization of adaptive sliding mode assisted disturbance observer and validation on inertially stabilized gimbal. In: 2024 9th International Conference on Control and Robotics Engineering (ICCRE); 2024 May 10–12; Osaka, Japan. p. 253–8.
3. Alkaar TA, Daw MS, Jamjom AF. Automated parking system using PLC technology. Int J Electr Eng and Sustain. 2024;2(3):35–46.
4. Liu Z, Xiong W, Xiong M. A large-scale scheduling method for multiple agile optical satellites. Comput Model Eng Sci. 2023;136(2):1143–63. doi:10.32604/cmes.2023.025452.
5. Alghyaline S. Arabic optical character recognition: a review. Comput Model Eng Sci. 2023;135(3):1825–61. doi:10.32604/cmes.2022.024555.
6. Alshammari FS, Hoque MF, Or-Roshid H, Nadeem M. Bifurcation analysis and bounded optical soliton solutions of the biswas-arshed model. Comput Model Eng Sci. 2023;135(3):2197–217. doi:10.32604/cmes.2023.022301.
7. Zhou G, Tang Y, Xie Y, Song R, Zhu Q, Zhou X. Calibration of fisheye camera with co-linear constraint of the main optical axis and epipolar line orthogonality-transverse axis. IEEE Sens J. 2024;24(12):19373–84. doi:10.1109/jsen.2024.3392810.
8. Marsocci V, Audebert N. Cross-sensor self-supervised training and alignment for remote sensing. IEEE J Sel Top Appl Earth Obs Remote Sens. 2025;18:12278–89. doi:10.1109/jstars.2025.3566457.
9. Strickland RN. Infrared techniques for military applications. In: Infrared methodology and technology. Boca Raton, FL, USA: CRC Press; 2023. p. 397–427.
10. Li X, Zhou X, Yan K. Technological progress for sustainable development: an empirical analysis from China. Econ Anal Policy. 2022;76(4):146–55. doi:10.1016/j.eap.2022.08.002.
11. Cao MQ, Li XY, Hou XH, Zhang G, Lei Y, Fu XH. Adjustment of optical axis consistency of spatial rotation in laser coupling. In: AOPC 2021: advanced laser technology and applications. Vol. 12060. Bellingham, WA, USA: SPIE; 2021. p. 377–82.
12. Niu J, Zhao Y, Wang C, Dong X, Fu R. Research on assembling and adjusting technology of aspherical refraction optical lens. In: Eighth Symposium on Novel Photoelectronic Detection Technology and Applications. Vol. 12169. Bellingham, WA, USA: SPIE; 2022. p. 464–9.
13. Demir U, Akgün G, Aküner MC, Demirci B, Akgun O, Akinci TC. Feature extraction and NN-based enhanced test maneuver deployment for 2 DoF vehicle simulator. IEEE Access. 2023;11(5):36218–32. doi:10.1109/access.2023.3266326.
14. Lee SM, Son H. Multi-sensor integration and fusion for control of multi-DOF spherical motion platform. Mechatronics. 2021;77(4):102593. doi:10.1016/j.mechatronics.2021.102593.
15. Zhang J, Liu S, Peng Y, Chen S, Yang J, Zhao X, et al. Research on multi-optical axis online compensation alignment method for space environment simulation system. Optics Express. 2024;32(21):36708–28. doi:10.1364/oe.538898.
16. Sun X, Zhu W, Du H, Chen W, Chen CC. Image-based fast finite-time target tracking control of onboard inertially stabilized camera platform. IEEE Trans Ind Electron. 2024;71(12):16409–18. doi:10.1109/tie.2024.3387063.
17. Başlar İ, Dursun M. Improving neural-network-based prediction models for misalignment in off-axis three-mirror anastigmat telescopes. Appl Optics. 2024;63(29):7747–55. doi:10.1364/ao.532008.
18. Lu Y, Sun B, Mei G, Zhao Q, Wang Z, Gao Y, et al. Integrated analysis of line-of-sight stability of off-axis three-mirror optical system. Photonics. 2024;11(5):461. doi:10.3390/photonics11050461.

19. Peterson J, Peng E, Burke C, Sembroski G, Cheng J. Deformation of optics for photon Monte Carlo simulations. Astrophys J. 2019;873(1):98. doi:10.3847/1538-4357/ab0418.
20. King E, Levin Y, Ottaway D, Veitch P. Modeling thermoelastic distortion of optics using elastodynamic reciprocity. Phys Rev D. 2015;92(2):022005. doi:10.1103/physrevd.92.022005.
21. Shen W, Lin W, Wu W, Wu H, Li K. Reinforcement learning-based task scheduling for heterogeneous computing in end-edge-cloud environment. Cluster Comput. 2025;28(3):179. doi:10.21203/rs.3.rs-4568055/v1.